Acta Crystallographica Section A
Foundations of Crystallography
ISSN 0108-7673

Received 19 July 2002
Accepted 6 December 2002

Structure of Ti_2P solved by three-dimensional electron diffraction data collected with the precession technique and high-resolution electron microscopy

Mauro Gemmi,[a]*† Xiaodong Zou,[a] Sven Hovmöller,[a] Andrea Migliori,[b] Marie Vennström[c] and Yvonne Andersson[c]

[a]Structural Chemistry, Stockholm University, SE-106 91 Stockholm, Sweden, [b]CNR Istituto IMM Sezione di Bologna, Area della Ricerca di Bologna, via Gobetti 101, I-40129 Bologna, Italy, and [c]Department of Material Chemistry, The Ångstrom Laboratory, SE-751 21 Uppsala, Sweden. Correspondence e-mail: mauro.gemmi@unimi.it

The crystal structure of Ti_2P has been analysed using electron diffraction and high-resolution electron-microscopy techniques. A new unit cell was found, the compound is hexagonal with a = 19.969 (1) and c = 3.4589 (1) Å. The structure was first solved in space group $P\bar{6}2m$ in projection using direct methods on electron diffraction data from the [001] zone axis. A three-dimensional solution was obtained using again direct methods but on a three-dimensional set of electron diffraction data recorded with the precession technique. Ti_2P is a distorted Fe_2P structure and, based on high-resolution images, it is possible to explain that the tripling of the unit cell is due to the ordering of P vacancies that reduces the symmetry to $P\bar{6}$.

1. Introduction

1.1. The Ti_2P structural problem

The structure solution of Ti_2P is quite an old structural problem. The first indications for a Ti_2P phase were reported by Biltz *et al.* (1938) and by Vereikina & Samsonov (1960), but the poor quality of their data prevented them giving any structure information on this new compound. A first structural model was proposed by Yeremenko & Listovnichy (1965). They claimed that Ti_2P is isomorphous with Fe_2P which at those times was considered to be trigonal [space group $P321$ (Hendricks & Kosting, 1930)] instead of hexagonal (space group $P\bar{6}2m$) as demonstrated later by Rundquist & Jellinek (1959). The corresponding unit cell in the hexagonal setting was a_{Fe_2P} = 6.715 and c = 3.462 Å. Further progress on the structure determination was made by Lundström & Snell who reported two different phases having composition close to Ti_2P but one richer in Ti and the other richer in P and both having a hexagonal unit cell with a = 11.5314 (15), c = 3.455 (9) Å and a = 11.5276 (18), c = 3.4580 (12) Å (Lundström & Snell, 1967; Snell, 1968). Since the c axis is very short and the ratio between the observed structure-factor amplitudes $F(hk0)/F(hk2)$ is constant within experimental error, it was possible to guess that the atoms are arranged on planes perpendicular to the c axis and $c/2$ apart. Using a Weissenberg camera, the Laue symmetry was proved to be $6/mmm$. Based on this information, Ti_2P was supposed to be a distorted Fe_2P-type structure with the hexagonal supercell ($a = 3^{1/2}a_{Fe_2P} \sim$ 11.53 Å) rotated 30° with respect to the unit cell of the underlying Fe_2P model. After that for several years there were no improvements until Carrillo-Cabrera in his PhD thesis (Carrillo-Cabrera, 1982) discovered, on films recorded with a Weissenberg camera, weak reflections that could be indexed only by tripling the unit cell along a_{Fe_2P} and b_{Fe_2P}. This gives an a parameter of nearly 20 Å. Unfortunately, the impossibility of growing good single crystals has prevented the structure solution with X-ray data so far.

1.2. Electron crystallography

During the last few years, it has been demonstrated that electron crystallography can be an alternative technique for structure resolution in difficult structural problems when only poor-quality X-ray data are available. Several complicated structures have been solved recently (Gemmi *et al.*, 2000; Weirich *et al.*, 2000) by applying direct methods to three-dimensional (3D) sets of electron diffraction (ED) data. In those studies, the ED intensities are considered kinematical and only a rough dynamical correction [ED intensity I_{khl} proportional to the structure-factor amplitudes $|F(hkl)|$] is taken into account in the second paper. These papers show that, even if the ED is dynamical, as a first attempt a kinematical approximation can give promising results. In fact, even though the reconstructed crystal potential is different from the real one, nevertheless it keeps peaks located in the correct

† Present address: Dipartimento di Scienze della Terra 'Ardito Desio', Sezione di Mineralogia, Università di Milano, via Botticelli 23, I-20133 Milano, Italy.

atomic positions (Sinkler *et al.*, 1998; Hu *et al.*, 2000; Weirich, 2001). The dynamical diffraction alters the relative heights of these peaks, so their labelling with the correct atomic species is not straightforward. However, this is not a peculiarity of ED only. The same problem arises when we try to solve a structure with powder X-ray diffraction (PXRD) data. The intensities are in this case not exactly proportional to the square modulus of the structure factors because the superimposition of the peaks prevents a faithful extraction. Nevertheless, structural solution with PXRD is commonly attempted and there are also algorithms for treating the problem of labelling (Altomare *et al.* 2002). Consequently, when only powder samples are available, electron crystallography should be considered as a possible technique. As well as with PXRD data, the structural solution is often difficult. Reliable kinematical intensities are not available and it is difficult to obtain a correct 3D set of data. Since the dynamical effects affect distinct zone axes differently, it is a problem to scale intensity data coming from different zone axes on the same scale. The final 3D set of reflections is affected by rescaling errors that can prevent the structure solution from succeeding. Therefore it is quite important to reduce the dynamical effects not only because the conventional structure-solution methods use the intensities as kinematical but also to obtain a consistent 3D set of data not perturbed by rescaling errors. The precession technique proposed for the first time by Vincent & Midgley (1994) seems to be a good candidate for collecting kinematical ED data (Gjønnes, 1997). A structure solution of Al_mFe with a 3D set of intensities recorded with the precession technique was obtained by J. Gjønnes *et al.* (1998). They showed that this technique gives intensities suitable for structure solution both with Patterson analysis and direct methods. K. Gjønnes *et al.* (1998) demonstrated that precessed data can be improved using a two-beam approximation *via* the Blackman formula (Blackman, 1939). Moreover, they introduced a further dynamical correction by applying the Bethe effective potential (Bethe, 1928). Precessed data are on one hand closer to a kinematical approximation, on the other they can be treated with suitable dynamical approximations without carrying out full dynamical calculations.

In summary, the recent successes of electron crystallography and the possibility of increasing the quality of the data with new methods of data collection as the precession technique have encouraged the authors to venture to solve the structure of Ti_2P with electron diffraction.

In this way, the hypothesis of tripling of the unit cell along the a_{Fe_2P} and b_{Fe_2P} axes has been confirmed and the structure has been solved in [001] projection with direct methods on a two-dimensional (2D) set of data collected in conventional selected-area electron diffraction (SAED). A three-dimensional solution was obtained with direct methods on a set of intensities recorded using the precession technique. The final model is a distorted Fe_2P structure. As suggested by the streaking observed in the SAED along (*hk*0) rows, the high-resolution electron-microscopy (HREM) images have shown that the structure is disordered on a very small scale. Furthermore, in the ordered regions the structure has a lower symmetry than $P\bar{6}2m$. It has been possible to obtain a matching between simulations and the images by reducing the symmetry to $P\bar{6}$ and creating P vacancies in the structure. This indicates that the superstructure arises as ordering of the P vacancies. The structure solution cannot reveal the ordering since the data are always averaged over an area bigger than the ordered domains.

2. Experimental

The sample was synthesized by reacting appropriate amounts of titanium rod turnings and lumps of red phosphorus with a claimed purity of 99.98 and 99.9%, respectively. The phosphorus lumps were placed in one end of a 30 cm long evacuated sealed quartz tube at 723 K and the titanium turnings in the other end at approximately 1070 K for one month. The product was melted in an arc furnace under argon atmosphere. According to X-ray powder diffraction photographs, the sample contained Ti_2P and small amounts of Ti_3P.

The samples for electron microscopy were prepared by mild grinding of the powder, suspension in butanol and deposition on a holey carbon film.

Standard electron diffraction investigations were performed on a JEOL 2000FX operating at 200 kV using photographic plates. The negatives were digitized using a Kite 12-bit CCD camera. The chemical microanalysis has been carried out on the same microscope using a Link energy-dispersive spectrometer (EDS).

For the precession technique, we collected the data on a CM30/T Philips electron microscope operating at 300 kV. The diffraction patterns were recorded on a Gatan Slow Scan CCD camera.

The HREM images were taken on an FEI/Philips Tecnai F30 ST operating at 300 kV equipped with a 2 K by 2 K Gatan Slow Scan CCD camera.

3. Electron diffraction data collection

3.1. Conventional SAED analysis

SAED patterns were recorded on photographic films and digitized using a Kite 12-bit CCD camera. Particular care was taken in finding very thin crystals and in placing the selected-area diaphragm partly outside the crystal in order to select only its thinnest region. Multiexposure series of 2, 4, 8, 16 s were taken for every zone axis in order to ensure that every reflection is not heavily saturated on at least one plate. After digitizing the negatives, the reflection intensities were extracted using the program *ELD* (Zou *et al.,* 1993). Data from different exposures were merged by calculating the average ratio between the corresponding non-saturated reflections present in the two plates. The scaling coefficients C_{resc} between adjacent exposures were always in the interval $1.9 < C_{resc} < 2.1$, *i.e.* close to the ideal value of 2.

3.2. Precession technique analysis

Vincent & Midgley proposed the precession technique for the first time in 1994 as a possible method for reducing dynamical effects in diffraction patterns and collecting a set of integrated intensities suitable for structure solution (Vincent & Midgley, 1994). The crystal is first oriented along a zone axis. Then, by using the upper scan coils, the beam is tilted and precessed around the optical axis on a conical surface having the vertex fixed on the specimen plane. At the same time, the lower scan coils descan the scattered electrons in antiphase with respect to the upper ones, such that a stationary diffraction pattern is obtained. As pointed out by Vincent & Midgley, this method can reduce at least the non-systematic dynamical interactions, since only very few strong reflections belonging to different rows are simultaneously excited during the precession cycle.

In the Philips CM30T microscope, no direct access to the scan coils is available. Consequently, the only way to precess the electron beam was to apply a suitable sinusoidal signal to the external Analog Interface Board. This signal digitalized by the board is processed by the CPU of the microscope which generates the desired scan and descan signals for the upper and lower scan coils, respectively. These special options are available only in the selected-area channelling-pattern (SACP) mode of the STEM configuration. The nanoprobe electron beam is formed into a small (500 Å) but parallel beam which is precessed on a cone surface whose vertex lies on the specimen.

The alignment of the microscope is very critical in the nanoprobe lens configuration and consequently, owing to difficulties in tuning the scanning, the beam is not steady at one point but is moving on the sample. The final diffraction pattern is usually recorded collecting diffracted electrons coming from an area of approximately 1000 Å in diameter.

The experimental intensity of reflection $\mathbf{g}$, $I_{\rm exp}(\mathbf{g})$, is integrated over the precession angle

$$I_{\rm exp}(g) = \int_0^{2\pi} I_g(\alpha)\,{\rm d}\alpha, \tag{1}$$

where $I_{\rm g}(\alpha)$ is the intensity of the reflection g (the square modulus of the g Fourier components of the electron exit wave function) when α is the angle between the vector g and the vector joining the central beam with the center of the Laue circle. As well explained in the articles of Gjønnes (1997) and K. Gjønnes *et al.* (1998), this integration can be transformed into an integration over the excitation error s_g since

$$2ks_g = -g^2 - 2gR\cos(\alpha),$$

where R is the radius of the Laue circle and k is the electron wave vector. By differentiating this we have

$$k\,{\rm d}(s_g) = gR\sin(\alpha)\,{\rm d}(\alpha).$$

If we consider that the strongest contribution to the integral (1) is given when the reflection g is near the Bragg condition, we can approximate $\sin(\alpha)$ as

$$\sin(\alpha) = [1 - (g/2R)^2]^{1/2}. \tag{2}$$

This does not depend on the precession angle any more and can be extracted from the integral giving

$$I_{\rm exp}(\mathbf{g}) \propto \{g[1 - (g/2R)^2]^{1/2}\}^{-1} \int_{-\infty}^{\infty} I_g(s_g)\,{\rm d}s_g, \tag{3}$$

where we have eliminated all the quantities that are constant and do not depend on g.[1] This expression is valid if the divergence of the beam can be neglected (Gjønnes, 1997). Expression (3) says that if the recorded intensities are corrected by a factor $C(g, R) = g[1 - (g/2R)^2]^{1/2}$ it is possible to gain access to the integral of the diffraction intensities over the excitation error. For thicknesses smaller than the extinction distance, this quantity is proportional to the square modulus of the structure factor $|F(g)|^2$ (kinematic approximation) whereas for thicker crystals a two-beam approximation is needed.

In this case, the integral in the second term of equation (3) becomes

$$\begin{aligned}\int_{-\infty}^{\infty} I_g(s_g)\,{\rm d}s_g &\propto |F(g)|^2 \int_{-\infty}^{\infty} \frac{\sin^2\{t[(\pi s_g)^2 + Q^2]^{1/2}\}}{(\pi s_g)^2 + Q^2}\,{\rm d}s_g \\ &= |F(g)|^2 (1/Q) \int_0^{Qt} J_0(2x)\,{\rm d}x \\ &\propto |F(g)| \int_0^{Qt} J_0(2x)\,{\rm d}x,\end{aligned} \tag{4}$$

where we have used the notation of Vainshtein (1964): J_0 is the Bessel function of order 0 and Q^{-1} is proportional to the extinction distance.[2] Formula (4) is known as the Blackman formula (Blackman, 1939). It should be remarked that the Blackman formula is quite imprecise if the reflection g is affected by strong systematic interactions. This holds for weak reflections that are higher orders of strong inner reflections (Cowley, 1975). Unfortunately, the precession does not reduce systematic n-beam dynamical interactions. In fact, while the Laue circle is sweeping the reciprocal space, all the reflections belonging to a row tangential to it are close to Bragg condition (Vincent & Midgley, 1994). This can cause problems with weak reflections at high angles. A possible way of considering n-beam effects is to replace $F(g)$ with an effective structure factor following Bethe's work (Bethe, 1928; Spence & Zuo, 1992). In any case, an insight on the thickness value is needed if we want to recover the structure-factor amplitude from the experimental intensities by the inversion of the integral (4).

A study carried out on known structures has shown that the kinematic approximation can be used only in the very rare cases when the crystal has a uniform thickness over a large area, like in a thin film prepared in cross section with ion milling. In general, instead, a linear correlation between $|F(g)|$

[1] The symbol $\propto$ means proportional to.
[2] In Vainshtein's notation, $Q = \lambda|F(g)/\Omega|$, where $F(g)$ is the structure factor and Ω is the unit-cell volume.

and the recorded intensity after correction for the precession geometry [equation (3)] has been observed (Gemmi *et al.*, 2002). This can be explained by the fact that, since the beam is moving over a large area of the sample (~1000 Å), the average thickness is clearly bigger than the extinction distance, nonetheless the precession diffraction geometry is reducing the dynamical scattering in such a way that two-beam is still a good approximation. Under this assumption, in the last integral of (4) it is possible to substitute the upper integration limit with ∞, obtaining

$$I_{\rm exp}(g)C(g,R) \propto \int_{-\infty}^{\infty} I_g(s_g)\,{\rm d}s_g \propto |F(g)| \int_0^{\infty} J_0(2x)\,{\rm d}x = \tfrac{1}{2}|F(g)|. \quad (5)$$

It must be recalled that since this expression is based on the Blackmann formula (4), for those reflections that are affected by strong systematic interactions this approximation is also imprecise.

The precessed ED patterns have been recorded using a Gatan CCD slow-scan camera with a multi-acquiring procedure. In order to avoid the saturation of the CCD and increasing the dynamical range, several short exposures (5 of 0.8 s each) were taken and added together in a buffer image. Then the dark current background integrated for the total exposure time was subtracted from this giving the final pattern. The tilt angle of the beam with respect to the optical axis was about 1° corresponding to a radius of the Laue circle of 0.9 Å^{-1}. This was the maximum angle reachable without significant distortions in the cone shape. The intensities extracted using the program *QED* (Belletti *et al.*, 2000) and corrected with the factor $C(g, R)$ were merged into a 3D data set using the average ratio between the intensities of the common row of reflections.

4. Structure analysis

In the powder X-ray patterns (PXRD), all the strongest peaks belonging to Ti_2P can be indexed with a hexagonal unit cell having a_{Fe_2P} = 6.646 (2) and c_{Fe_2P} = 3.458 (1) Å corresponding to the undistorted Fe_2P model. After removing a few peaks related to the Ti_3P impurity, only two very weak superstructure peaks are still present. This suggested a deeper analysis of the sample using electron diffraction.

4.1. Structure solution by 2D SAED

SAED patterns reveal that the unit cell reported in the literature (Lundström & Snell, 1967) is just a first-order superstructure while that reported by Carrillo-Cabrera (1982) is the correct unit cell. From the [001] projection (Fig. 1*a*), it is evident that the real structure has a tripling of the unit cell along both a_{Fe_2P} and b_{Fe_2P} as shown by the appearance of two weak spots between the strongest one in the (h00) and (0k0) rows. To check the unit cell, six diffraction patterns in different zone axes were taken and with the unit-cell parameters set to a = 19.969 (1) and c = 3.4589 (1) Å (these values were obtained from a refinement on PXRD data) all of them can be indexed properly. The SAED patterns also show streaks along (h00) and (hh0) rows, indicating disorder on the *ab* plane (see Figs. 1*b*, *c*).

Since in PXRD the information on the superstructure is almost absent and pure Ti_2P samples are not available, SAED data were used to solve the structure. A first attempt to solve the structure in [001] projection was tried by using the direct-methods program *SIR97* (Altomare *et al.*, 1999). Following the

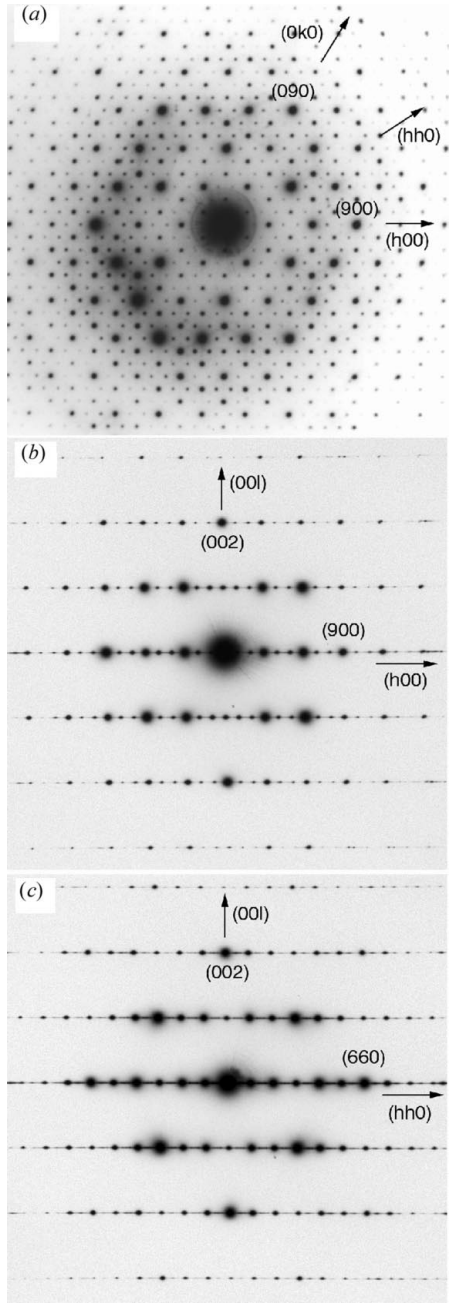

Figure 1
SAED patterns of Ti_2P. (*a*) [001] zone axis. Note that the rows of reflections parallel to (h00) and (hh0) both have a sequence of one strong and two weak spots indicating superstructures. (*b*) [010] zone axis. (*c*) [$\bar{1}$10] zone axis. The streaks along (h00) and (hh0) due to defects are evident and strong in the last two projections.

previous literature, the structure should be an Fe_2P distorted model, and thus it should be possible to separate all the atoms by looking down the *c* axis. For the solution, a set of 79 independent *hk*0 reflections was processed. Among all possible space groups within the 6/*mmm* Laue class, only those without translation symmetry elements have been considered because no extinction was detected. The dynamical approximation $|F_{hkl}| \propto I_{hkl}$ proposed by Vainshtein (1964) and successfully used in a recent paper (Weirich *et al.* 2000) was used and the random procedure for phasing reflections was chosen. A reasonable solution was obtained only for the space group $P\bar{6}2m$ with a final *R* value of 27.3%. The corresponding potential map is shown in Fig. 2. This is a distorted Fe_2P-type structure, but with three P atoms in the $z = 0$ plane in special positions missing, as can be seen by comparing the map with the model of Fe_2P on the left of Fig. 2. The total unit-cell content is 54 Ti and 21 P. There is also a good agreement between the height of the peaks and the chemical species occupying the sites. In fact, the 12 strongest peaks correspond to the 12 Ti atoms in the asymmetric unit. The presence of disorder on the *ab* plane suggests that the vacancies of P atoms shown by the potential map could be real and not due to the quality of our data. However, if this is the case, the composition should be $Ti_{18}P_7$, quite close to a Ti:P ratio of 2.5:1. In order to check this, EDS analysis has been carried out using Ti_3P as an internal standard. The average composition obtained by measuring ten different crystals gives an atomic percentage at.(Ti) = (67±2)%, very close to the ideal composition of Ti_2P. Since there are 54 Ti atoms in the unit cell, EDS analysis indicates that the number of vacancies, if they are present, should be around three P atoms per unit cell and not six as obtained in the structure solution.

To investigate this problem more thoroughly and to see if the atoms are really distributed on planes perpendicular to the *c* axis and separated *c*/2 apart like in the Fe_2P model, a 3D solution attempt was made. The 3D set of intensities was obtained by merging six different zone axes ([100], [001], [1$\bar{1}$0], [01$\bar{1}$], [0$\bar{1}$2], [$\bar{1}$13]). Unfortunately, the *R* values calculated by comparing the rescaled intensities along the common rows of reflections and the original ones were always higher than 30%, indicating that the data were not homogeneous. As a consequence of this, it was impossible to find a solution with a 3D data set of SAED intensities.

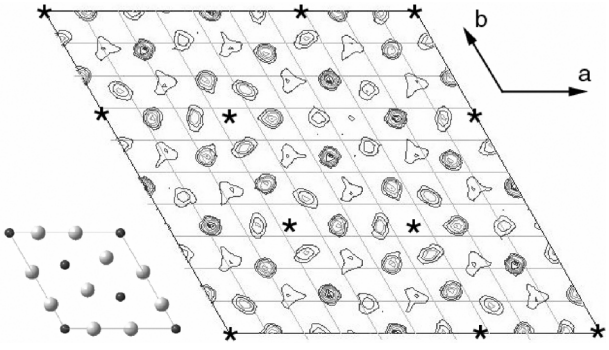

Figure 2
Potential map obtained with the program *SIR97* from the two-dimensional [001] data set (see Fig. 1*a*). For comparison, the Fe_2P-type structure is inserted on the left (small dark spheres P, large light spheres Fe). Positions of missing P atoms are marked by ★.

4.2. Structure solution by precession technique

As a further step in the structure analysis, electron diffraction data were collected using the precession technique. If the dynamical effects could be reduced, a more reliable 3D set of intensity could be obtained. In Fig. 3, the [001], [100] and [1$\bar{1}$0] ED patterns taken with this technique are shown. The

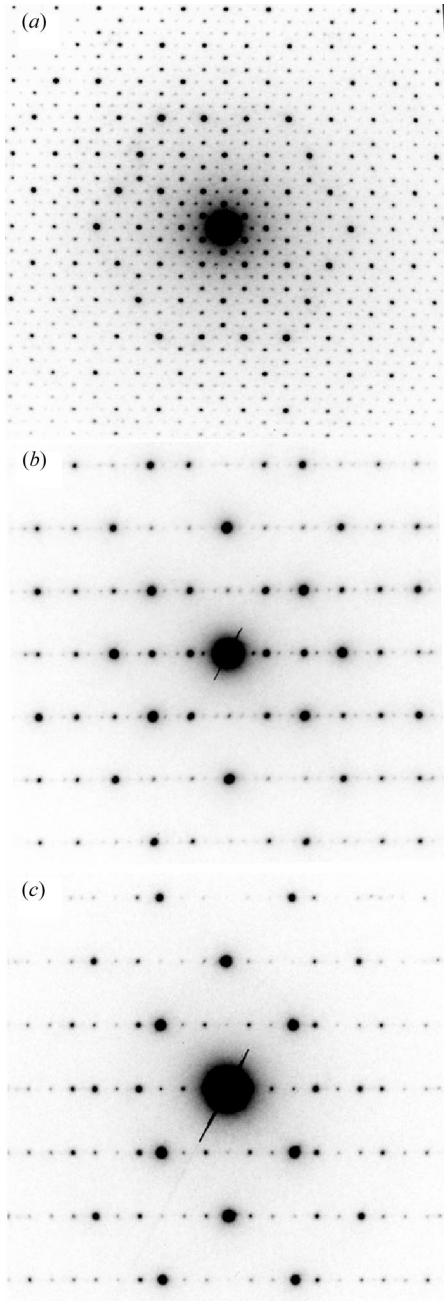

Figure 3
Same ED patterns as in Fig. 1 but taken with the precession technique. (*a*) [001] zone axis. (*b*) [100] zone axis. (*c*) [1$\bar{1}$0] zone axis.

Table 1
Crystal data of Ti_2P without P vacancies.

Formula sum	$Ti_{54}P_{27}$
Formula weight	3421.81
Crystal system	Hexagonal
Space group	$P\bar{6}2m$ (No. 189)
Unit-cell dimensions (Å)	a = 19.969 (1), c = 3.4589 (1)
Cell volume (Å^3)	1194.49 (9)
Density, calculated (g cm^{-3})	4.778

intensities corrected with the factor $C(g, R)$ were merged using the average ratio between the intensities of the common row of reflections. First, [100] and [001] were rescaled using the (0k0) row, then the [1$\bar{1}$0] was brought on their scale using the (00l) row. The R values were in this case 13 and 22%, respectively, much better than those obtained from the SAED data. The final set of 3D data formed by 200 independent reflections was phased using direct methods with the program *SIR97*. The approximation (5) was applied. A reasonable solution was found in space group $P\bar{6}2m$ by taking into account only 98 independent reflections out of 200 up to 1.3 Å resolution. If more reflections were added, several atoms were missing or located too close to other sites, probably because the Blackman formula is too approximate. This is due to strong systematic interactions between intense inner reflections and weak reflections at high angle (see §3.2). Furthermore, these same reflections have smaller extinction distances and consequently a higher thickness is needed for approximation (5) to hold.

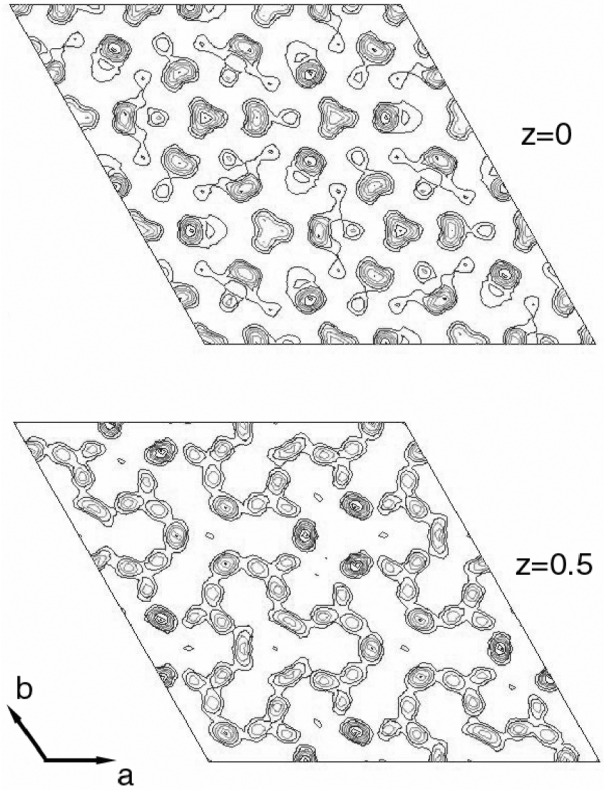

Figure 4
Slices in the planes normal to the c axis of the potential map obtained with the program *SIR97* using the precessed data. Top: z = 0; bottom: z = 0.5.

Table 2
Atomic positions found by *SIR97* on precessed data.

The errors reported are calculated on the basis of one cycle of refinement. In the fourth column, the differences in Å between the corresponding positions found using SAED data.

Atom	Multiplicity, Wyckoff symbols	x	y	z	D (Å)
Ti1	6(k)	0.427 (6)	0.093 (6)	1/2	0.11
Ti2	3(g)	0.239 (8)	0	1/2	0.05
Ti3	6(j)	0.330 (6)	0.133 (6)	0	0.20
Ti4	3(f)	0.472(8)	0	0	0.42
Ti5	3(g)	0.098 (8)	0.098 (8)	1/2	0.12
Ti6	6(k)	0.755 (5)	0.424 (7)	1/2	0.10
Ti7	3(f)	0.136 (8)	0	0	0.51
Ti8	6(j)	0.878 (6)	0.545 (6)	0	0.08
Ti9	6(j)	0.800 (7)	0.330 (8)	0	0.39
Ti10	3(f)	0.206 (7)	0.206 (7)	0	0.03
Ti11	3(g)	0	0.590 (7)	1/2	0.18
Ti12	6(k)	0.335 (6)	0.245 (6)	1/2	0.11
P1	2(c)	2/3	1/3	0	–
P2	1(a)	0	0	0	–
P3	3(f)	0.33 (1)	0	0	0.16
P4	6(k)	0.444 (7)	0.23 (1)	1/2	0.18
P5	6(k)	0.225 (7)	0.117 (9)	1/2	0.14
P6	6(k)	0.55 (1)	0.108 (7)	1/2	0.16
P7	3(f)	0.33 (1)	0.33 (1)	0	–

As expected, the atoms are located on two planes, one at z = 0 and the other at z = 0.5 in a distorted Fe_2P model. A section of the potential map on these two planes and the final model obtained using the coordinates given by *SIR97* are shown in Figs. 4 and 5, respectively. Compared to the SAED solution, the map is more noisy, the final R value is also higher (36%), but all the P atoms in the z = 0 plane are now visible and a complete 3D solution is available. The crystal data, atomic parameters and the differences in the positions between the

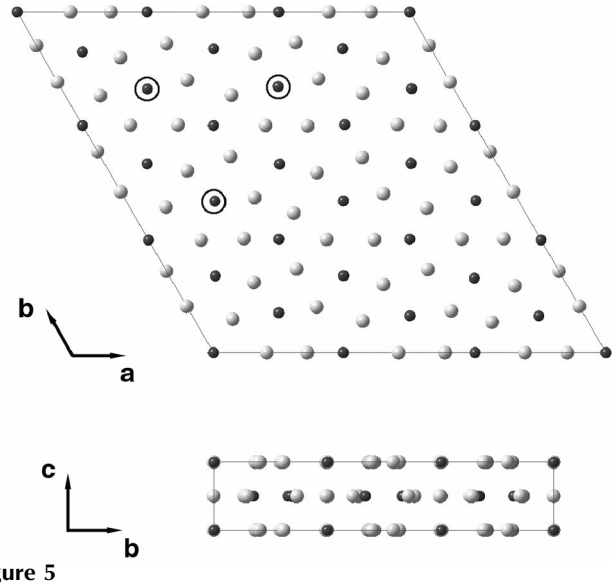

Figure 5
Structure of Ti_2P obtained with precessed data (Ti: light grey spheres; P: dark grey spheres). Top: [001] projection; bottom: [10$\bar{0}$] projection. The circles indicate the P atoms removed in the $P\bar{6}$ model of the superstructure.

solutions obtained with the SAED and the precessed intensities are given in Tables 1 and 2.[3] Three Ti atoms (Ti4, Ti7, Ti9) differ by more than 0.39 Å in the two solutions but the Ti—P distances obtained with precessed data are more reasonable. Only four Ti—P distances are smaller than 2.4 Å (see Table 3), whereas in the SAED case five P sites have this problem and two of them are even shorter than 2.3 Å. The quality of the SAED data is not good enough to give a complete explanation of what causes the superstructure. Only small displacements from the ideal positions of the Fe_2P model are seen in the solution and these are below the sensitivity of the method. The two solutions are contradictory about the presence of P vacancies in the structure. The amount of disorder shown by the streaks in the [100] and [1$\bar{1}$0] zone axes suggests that our model describes only the average structure. To clarify this point, high-resolution electron-microscopy images (HREM) were taken.

4.3. Structure analysis by HREM imaging

The HREM analysis shows that the structure is very often disordered and the superstructure corresponding to the 19.97 Å unit cell is not always visible. A typical situation is shown in Fig. 6. Here the crystal is oriented along [100] and from the Fourier transform of the image only the spots belonging to the Fe_2P model unit cell (a_{Fe_2P} = 6.64 Å) can be seen, whereas the superstructure reflections are replaced by streaks. Ordered and disordered regions alternate inside the same crystal on a very small scale. A few hundred nanometres away from the area shown in Fig. 6, a very well ordered area was found on the same crystal (see Fig. 7). In the thicker region (Fig. 7*b*), the superstructure is quite clear but the symmetry is different from what was expected. In space group $P\bar{6}2m$, this projection should have *p2mm* symmetry but the image shows only one mirror perpendicular to the *c* axis. Thus it was not possible to reproduce the correct contrast by simulating the image with the previous model and the symmetry must be reduced to $P\bar{6}$ by removing the mirror normal to the *ab* plane. Since every attempt to solve the structure using this space group failed, we guessed that the Ti atoms (which are the strongest scatterers) follow quite well the $P\bar{6}2m$ model and the symmetry reduction is mainly due to some ordering of P vacancies. By looking at the contrast in the image and taking into account the results of EDS analysis, we built up a model using the structure obtained previously but with three P atoms in the unit cell removed (they are indicated in Fig. 5 by circles). In this way, the number of P atoms in the layer z = 0.5 is closer to the number of P atoms in the plane z = 0. There are 9 P at z = 0 and 15 P at z = 0.5. The chemical composition becomes Ti_9P_4 corresponding to at.(Ti) = 69% in atomic percentage, which is still within the error of the EDS microanalysis results. If these are the only P-vacancy sites then the symmetry is reduced to $P\bar{6}$ since there is no longer a mirror parallel to the [110] direction and normal to the *ab* plane. In Fig. 7, a comparison between the simulated and experimental images for a thin and a thicker region of the crystal are displayed. A quite good agreement is obtained in both areas using the same defocus values (as it should be since they correspond to different parts of the same image).

In the other fundamental projection, [001], the crystals are always very thick and in the narrow thin region near the edge only the 11.5 Å periodicity can be detected (see inset of Fig. 8). Furthermore, these spots are always very weak and in certain areas only the Fe_2P-structure reflections can be seen in

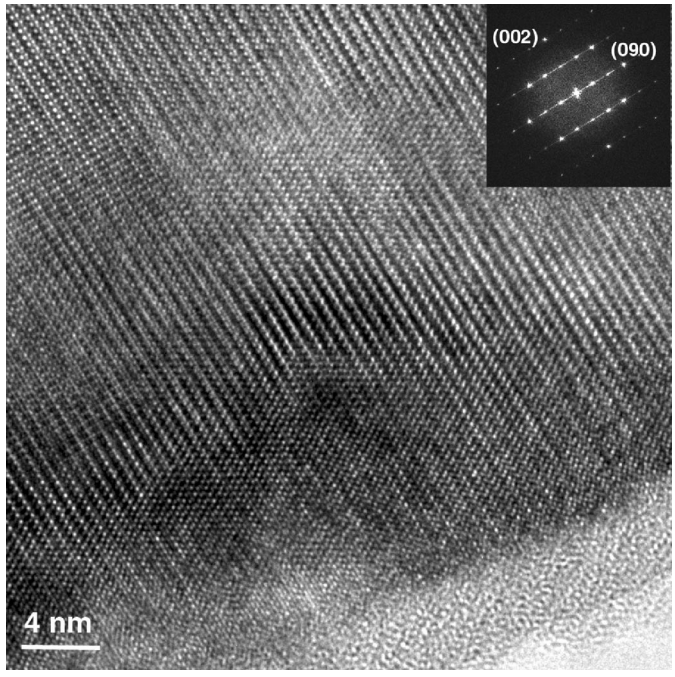

Figure 6
HREM image of a disordered region of Ti_2P in projection [100]. In the inset, the Fourier transform of the image is displayed: between the spots corresponding to the a = 6.64 Å unit cell the superstructure reflections are replaced by streaks owing to the disorder.

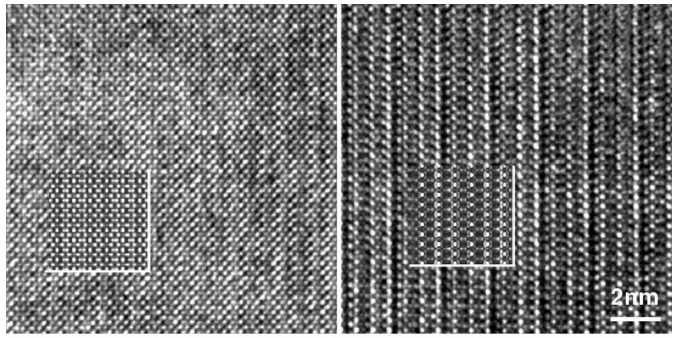

Figure 7
HREM image of Ti_2P taken in [100] projection on an ordered region of the sample. (*a*) Region of the image close to the edge of the crystal where the thickness is smaller. The inset shows a simulation calculated using the $P\bar{6}$ model for a thickness of 40 Å and a defocus of −80nm. (*b*) Thicker region of the same crystal. The inset shows a simulation calculated using the $P\bar{6}$ model for a thickness of 260 Å and the same defocus of −80 nm (as it should be since the two pictures belong to the same image).

[3] Supplementary data for this paper are available from the IUCr electronic archive (Reference GC0039). Services for accessing these data are described at the back of the journal.

Table 3
Interatomic distances (in Å) in Ti_2P calculated on the basis of the atomic positions given in Table 2.

The number before the second atom indicates the number of symmetry-equivalent positions of the second atom having the reported distance from the first atom.

Ti1—1Ti1	3.21 (15)	P1—6Ti6	2.49 (6)
Ti1—1Ti2	3.25 (20)	P1—3Ti9	2.71 (16)
Ti1—2Ti3	2.99 (17)		
Ti1—2Ti4	2.99 (15)	P2—6Ti5	2.61 (8)
Ti1—2Ti9	2.72 (10)	P2—3Ti7	2.72 (16)
Ti2—4Ti3	2.92 (8)	P3—2Ti2	2.51 (18)
Ti2—2Ti7	2.69 (17)	P3—4Ti1	2.57 (10)
		P3—2Ti3	2.66 (16)
Ti3—2Ti12	2.79 (14)	P3—1Ti4	2.84 (25)
Ti4—2Ti11	2.92 (14)	P4—1Ti6	2.40 (25)
		P4—1Ti12	2.34 (22)
Ti5—2Ti5	3.39 (20)	P4—1Ti1	2.58 (24)
Ti5—4Ti7	2.98 (18)	P4—2Ti8	2.61 (17)
Ti5—2Ti10	2.76 (11)	P4—2Ti9	2.70 (19)
		P4—2Ti3	2.74 (11)
Ti6—2Ti6	3.10 (17)		
Ti6—2Ti8	2.99 (9)	P5—1Ti2	2.49 (21)
Ti6—Ti9	3.00 (19)	P5—2Ti3	2.61 (15)
Ti6—2Ti9	2.87 (18)	P5—1Ti5	2.37 (22)
		P5—2Ti7	2.73 (10)
Ti8—2Ti11	2.75 (8)	P5—2Ti10	2.64 (19)
Ti8—2Ti12	2.76 (13)	P5—1Ti12	2.40 (14)
Ti10—4Ti12	2.87 (14)	P6—1Ti1	2.32 (24)
		P6—2Ti4	2.59 (8)
Ti11—2Ti12	2.86 (19)	P6—1Ti6	2.57 (14)
		P6—2Ti8	2.81 (19)
Ti12—1Ti12	3.11 (21)	P6—2Ti9	2.69 (19)
		P6—1Ti11	2.65 (23)
		P7—2Ti8	2.47 (26)
		P7—1Ti10	2.47 (17)
		P7—2Ti11	2.35 (10)
		P7—4Ti12	2.46 (19)

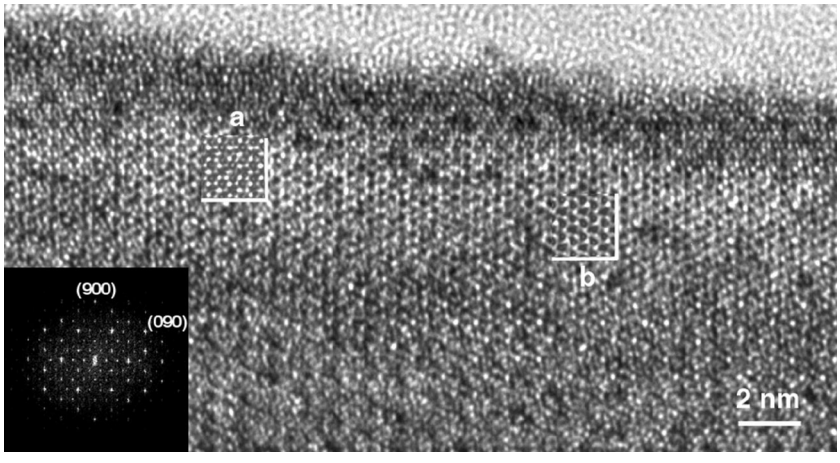

Figure 8
HREM image of Ti_2P taken in projection [001]. In the inset on the left, the Fourier transform of this area is displayed: only the spots corresponding to the 11.5 Å unit cell are visible. A comparison with simulated images is shown: (*a*) simulation calculated on the basis of the $P\bar{6}$ model for a thickness of 220 Å and defocus of −120nm; (*b*) simulation calculated on the basis of the $P\bar{6}2m$ model for a thickness of 240 Å and defocus of −130 nm.

the Fourier transform. The smallest details, like the faint dots in the middle of the distorted hexagons, do not follow a definite periodicity but seem to have a random distribution indicating that the structure is not completely ordered. The simulated images using both the $P\bar{6}$ and the $P\bar{6}2m$ models reproduce the contrast quite well but in different regions of the same image. By comparing the simulation with the structure, it can be seen that the dots in the center of the distorted hexagons are superimposed on P-atom sites. Since their distribution is irregular, this is a further indication that the order or disorder in the structure is connected to the order or disorder in the P vacancies. Moreover, this order can change on a very small scale. Over a distance of 100 Å, the contrast can change from the $P\bar{6}$ to the $P\bar{6}2m$ simulated image.

5. Discussion

The structure analysis of Ti_2P is quite a difficult problem since single crystals are not available and powder diffraction data show only the features of the average structure and the weak superstructure reflections are not visible. Furthermore, the crystals are ordered in nanometric domains and often show large disordered areas as the HREM images have confirmed. This is a typical case when electron crystallography is the most effective technique since the structural problem requires an analysis on a small scale of the order of several hundreds of ångströms.

The structure analysis by electron diffraction has shown that Ti_2P is a three times superstructure of the Fe_2P model along each of the a_{Fe_2P} and b_{Fe_2P} axes. Both the solutions obtained in 2D with conventional SAED data and with precessed data demonstrate that the Ti atoms follow quite well the Fe_2P model with $P\bar{6}2m$ symmetry and only small distortions are detected. For the P sites, the results are not completely clear. In the SAED solution, three P atoms in the asymmetric unit are missing. Moreover, the small displacements of the Ti atoms with respect to the ideal Fe_2P model are not big enough to justify the tripling of the unit cell. The problem in localizing the P atoms lies in the fact that they are weaker scatterers than Ti and that the quality of our data is poor. This is due to two main reasons. The first reason is dynamical scattering: when it was possible to reduce it with the precession technique all the possible P sites could be found. The second reason is the disorder. As can be seen by the diffraction patterns taken in [100] and [$1\bar{1}0$] projections, the disorder is present on a very small scale and it produces quite strong streaks along the (*h*00) and (*hh*0) rows of reflections. Furthermore, the HREM images confirm that on the same crystal ordered and disordered areas can be present and normally they have sizes of around 1000 Å. If this is the case, what we see in diffraction is an average situation where the diffraction

coming from ordered and disordered areas are superimposed. This may explain why it is impossible to solve the structure in the low-symmetry space group $P\bar{6}$ but possible in $P\bar{6}2m$, which is the average symmetry.

HREM images of the ordered areas in the [100] projection suggest how to build a model for the superstructure. They do not show *p2mm* symmetry but only *pm* symmetry, indicating that the symmetry must be reduced. A good matching between the experimental and simulated images is obtained if three P atoms per unit cell are taken away from the Fe_2P distorted solution and the symmetry is reduced to $P\bar{6}$. The tripling of the unit cell is then due to ordering of the P vacancies and not only to distortions of the Fe_2P model. However, other ordered structures seem to be possible. From some areas of the HREM images in [001], even if only the reflections corresponding to the 11.51 Å unit cell are present, the best agreement with the simulations is obtained with the $P\bar{6}2m$ complete model, whereas in other areas the vacancy model seems to match better. Therefore, we expect that this structure can have different ways of arranging the P atoms. There are Ti-richer regions where the superstructure appears as ordering of the P vacancies and P-richer regions where all the P sites are occupied and $P\bar{6}2m$ is the correct symmetry. In this last case, probably the correct unit cell is the original 11.5 Å or at least the distortions giving the tripling along a_{Fe_2P} and b_{Fe_2P} are so small that the corresponding spots are not visible in the Fourier transform of the image. These two ways of arranging P atoms might also explain the existence of Ti-richer and P-richer Ti_2P reported in the literature (Lundström & Snell, 1967; Snell, 1968; Carrillo-Cabrera, 1982).

Since the structure of this compound is changing from ordered to disordered type over distances of just a few nanometres, the structure refinement using powder X-ray diffraction data was problematic. In PXRD, all the superstructure reflections but two are invisible. Furthermore, it has been impossible to obtain pure phase samples and always a small amount of Ti_3P was present. The refinement of the $P\bar{6}$ model is unstable whereas for the $P\bar{6}2m$ model a final refined model can be obtained but the distances between several Ti and P atoms are too short to be correct. In both cases, the final R values are too high to trust the refinement. As already pointed out, this is due to the small dimension of the ordered domains with respect to X-ray coherence length. The analysis of powder neutron diffraction data is in progress.

6. Conclusions

The results obtained in this paper are a further proof that the precession technique can be used to collect high-quality 3D sets of ED diffraction intensities for structure solution with direct methods. Even if the dynamical scattering is not completely eliminated, its effect can be treated with a two-beam approximation integrated over a wide range of diffraction conditions. The obtained intensities are then proportional to the amplitudes of the corresponding structure factors. This allows merging of data from different zone axes using the intensity along common rows of reflections. The same procedure with normal SAED data is more difficult. Improvements in the control of the beam during the precession and the possibility of having small parallel beams with high brightness (using field-emission gun TEM) can reduce the area over which the beam is moving. In this way, data much closer to kinematical approximation might be collected. In the case of structures ordered on a small scale, more homogeneous sets of data may be obtained. This problem has been overcome in our paper by combining the solution obtained by direct methods with high-resolution electron microscopy. The matching between experimental and simulated images was used to check the model of P-vacancy order.

All attempts to refine the structure assuming kinematical scattering failed, probably because the data are still affected by residual dynamical effects as explained in the text. Consequently, the refinement must include dynamical effects in the procedure. A least-squares method coupled with the multislice algorithm recently proposed by Jansen *et al.* (1998) seems to be a possible way out of the problem. In that procedure, dynamical effects are not corrected but used to improve the structure solution obtained.

In summary, the precession technique increases the quality of electron diffraction data and reduces the gap between electron crystallography and X-ray crystallography. In the future, the electron microscope will be used more often by crystallographers as an instrument for structure solution.

The authors thank Jun Lu of Materials Science Division, Uppsala University, for useful discussions and technical support.

References

Altomare, A., Burla, M. C., Camalli, M., Cascarano, G. L., Giacovazzo, C., Guagliardi, A., Moliterni, A. G. G., Polidori, G. & Spagna, R. (1999). *J. Appl. Cryst.* **32**, 115–119.
Altomare, A., Giacovazzo, C., Ianigro, M., Moliterni, A. G. G. & Rizzi, R. (2002). *J. Appl. Cryst.* **35**, 21–27.
Belletti, D., Calestani, G., Gemmi, M. & Migliori, A. (2000). *Ultramicroscopy*, **81**, 57–65.
Bethe, H. (1928). *Ann. Phys. (Leipzig)*, **87**, 55–12.
Biltz, W., Rink, A. & Wiechmann, F. Z. (1938). *Z. Anorg. Allg. Chem.* **238**, 395.
Blackman, M. (1939). *Proc. R. Soc. London Ser. A*, **173**, 68.
Carrillo-Cabrera, W. (1982). PhD thesis, Uppsala Uniiversity. Uppsala, Sweden.
Cowley, J. M. (1975). *Diffraction Physics.* Amsterdam: North Holland.
Gemmi, M., Calestani, G. & Migliori, A. (2002). In *Advances in Electron Microscopy and Diffraction*, edited by P. G. Merli, M. V. Antisari & G. Calestani. Vol. 123 of *Advances in Imaging and Electron Physics* Series. New York: Academic Press.
Gemmi, M., Righi, L., Calestani, G., Migliori, A., Speghini, A., Santarosa M. & Bettinelli, M. (2000). *Ultramicroscopy*, **84**, 133–142.
Gjønnes, J., Hansen, W., Berg, B. F., Runde, P., Cheng, Y. F., Gjønnes, K., Dorset, D. L. & Gilmore, C. J. (1998). *Acta Cryst.* A**54**, 306–319.
Gjønnes, K. (1997). *Ultramicroscopy*, **69**, 1–11.
Gjønnes, K., Cheng, Y. F., Berg, B. S. & Hansen, W. (1998). *Acta Cryst.* A**54**, 102–119.
Hendricks, S. B. & Kosting, P. R. (1930). *Z. Kristallogr.* **74**, 511.
Hu, J. J., Chukhovskii, F. N. & Marks, L. D. (2000). *Acta Cryst.* A**56**, 458–469.

Jansen, J., Tang, D., Zandbergen, H. W. & Schenk, H. (1998). *Acta Cryst.* A**54**, 91–101.
Lundström, T. & Snell, P. O. (1967). *Acta Chem. Scand.* **21**, 1343–1352.
Rundquist, S. & Jellinek, F. (1959). *Acta Chem. Scand.* **13**, 425–432.
Sinkler, W., Bengu, E. & Marks, L. D. (1998). *Acta Cryst.* A**54**, 591–605.
Snell, P. O. (1968). *Acta Chem. Scand.* **22**, 1942–1952.
Spence, J. C. H. & Zuo, J. M. (1992). *Electron Microdiffraction.* New York: Plenum Press,
Vainshtein, B. K. (1964). *Structure Analysis by Electron Diffraction.* New York: Pergamon Press.
Vereikina, L. L. & Samsonov, G. V. (1960). *Zh. Neorgan. Khim.* **5**, 1888.
Vincent, R. & Midgley, P. A. (1994). *Ultramicroscopy*, **53**, 271–282.
Weirich, T. E. (2001). *Acta Cryst.* A**57**, 183–191.
Weirich, T. E., Zou, X. D., Ramlau, R., Simon, A., Cascarano, G. L., Giacovazzo, C. & Hovmöller, S. (2000). *Acta Cryst.* A**56**, 29–35.
Yeremenko, V. N. & Listovnichy, V. E. (1965). *Dopov. Akad. Nauk Ukr. RSR*, **9**, 1176.
Zou, X., Sukharev, Y. & Hovmöller, S. (1993). *Ultramicroscopy*, **49**, 147–158.